



Statistical Study of Coronal Mass Ejection Source Locations: Understanding CMEs Viewed in Coronagraphs

Yuming Wang, Caixia Chen, Bin Gui, Chenglong Shen, Pinzhong Ye, and S. Wang

KLBPP, School of Earth & Space Sciences, University of Science & Technology of China, Hefei, Anhui 230026, China;

Contact: [ymwang@ustc.edu.cn](mailto:yumwang@ustc.edu.cn)

Contents

1	Introduction	1
2	Data Preparation	2
3	Statistical Results of Source Locations	3
3.1	Distribution of CME Source Locations	3
3.2	Correlations between CME Source Locations and Apparent Properties	5
4	Inferences and Implications	6
4.1	Missing Rate of CMEs	6
4.1.1	Visibility in EIT	6
4.1.2	Visibility in LASCO	7
4.1.3	Invisible Front-side CMEs	7
4.2	Mass of CMEs	8
4.3	Causes of Halo CMEs	9
4.3.1	Halo vs. Non-halo CMEs	9
4.3.2	Limb vs. On-disk CMEs	10
4.4	Deflections of CMEs	10
4.4.1	Statistical Results and Classification	10
4.4.2	Interpretation and Exceptions	12
5	Concluding Remarks	13

Abstract. How to properly understand coronal mass ejections (CMEs) viewed in white-light coronagraphs is crucial to many relative researches in solar and space physics. The issue is now particularly addressed in this paper through studying the source locations of all the 1078 LASCO CMEs listed in CDAW CME catalog during 1997 – 1998 and their correlation with CMEs’ apparent parameters. By manually checking LASCO and EIT movies of these CMEs, we find that, except 231 CMEs whose source locations can not be identified due to poor data, there are 288 CMEs with location identified on the front-side solar disk, 234 CMEs appearing above solar limb, and 325 CMEs without evident eruptive signatures in the field of view of EIT. Based on the statistical results of CMEs’ source locations, four physical issues, including (1) the missing rate of CMEs by SOHO LASCO and EIT, (2) the mass of CMEs, (3) the causes of halo CMEs and (4) the deflections of CMEs in the corona, are exhaustively analyzed. It is found that (1) about 32% of front-side CMEs can not be recognized by SOHO, (2) the brightness of a CME at any heliocentric distance is roughly positively correlated with its

speed, and the CME mass derived from the brightness is probably overestimated, (3) both projection effect and violent eruption are the major causes of halo CMEs, and especially for limb halo CMEs, the latter is the primary one, (4) most CMEs deflected towards equator near the solar minimum, and these deflections can be classified into three types, the asymmetrical expansion, non-radial ejection, and the deflected propagation.

1 Introduction

Coronal mass ejections (CMEs) are recognized as transient bright features in the field of view (FOV) of white-light coronagraphs. However, their apparent properties/behaviors manifested in coronagraphs may not reflect what the CMEs actually should be, as observations of coronagraphs have at least three intrinsic limitations. The first one comes from the projection effect. All the three-dimensional information is embedded in two-dimensional images. Thus the position or speed of a CME measured in coronagraphs is only the projection of real position or speed on the plane of the sky, the shape of a CME depends on the angle of view, and the brightness recorded is an integral of the photons scattered by free electrons along the line-of-sight. The second one, we called occulting effect, is due to the occulting disk, which is used by coronagraphs to block the photons directly emitted from the photosphere. It was clearly pointed out by *Howard et al.* [1982] that two identical CMEs originating from the solar limb and disk-center, respectively, will look much different. The time and heliocentric distance of the disk-center CME entering the FOV of a coronagraph will be later and farther than those of the limb CME. It will further cause the disk-center CME fainter and diffuser than the limb CME. The third one is because of the Thomson scattering effect [e.g., *Hundhausen*, 1993; *Andrews*, 2002; *Vourlidas and Howard*, 2006]. This effect results in a so-called Thomson sphere, on which the plasma material is the most visible.

Moreover, in most popular coronagraph images, the inner corona is hidden behind the occulting disk. For example, the occulting disk size of the coronagraph LASCO/C2 onboard the SOHO spacecraft is $2 R_S$, and it is $1.4 R_S$ for the coronagraph COR1 onboard the STEREO twin spacecraft. Thus, we are blind to the CME behavior in the region covered by the occulting disk, where the CME propagation trajectory may change significantly. Here, we use the term ‘deflec-

tion' for the behavior of CME's non-radial ejection and/or propagation. It is an important factor for space weather. As early as 1986, *MacQueen et al.* had found the CME deflections in latitudinal direction by measuring 29 CMEs observed by the Skylab. *Gopalswamy et al.* [2000a] discussed the non-radial propagation of the 1997 December 14 CME and pointed out that such a phenomenon clearly implied the constraint of the complex multi-polar structures surrounding the CME [*Webb et al.*, 1997; *Gopalswamy et al.*, 2004]. With more CME events detected by LASCO during 1996 to 2002, *Cremades* and coworkers carried out a statistical study on their defined 'structured' CMEs. They found that many CMEs do not propagate radially with respect to their source locations, and the neighboring and/or polar coronal holes played a major role in causing the deflections of CMEs [*Cremades and Bothmer*, 2004; *Cremades et al.*, 2006].

The presence of these effects requires us to be very careful when we interpret the observed bright features in coronagraphs. Only white-light images from coronagraphs are not enough. The information of the solar source locations of all CMEs is necessary. There have been some efforts except for the previously mentioned work about CME deflections. *Yashiro et al.* [2005] investigated 1301 X-ray flares with intensity larger than C3 and their associations with CMEs, and found that about 14% of white-light CMEs were missed by LASCO. The statistically study of 9224 LASCO CMEs from 1996 to 2004 by *Lara et al.* [2006] suggested that halo CMEs are different from normal CMEs, which can not be merely explained by projection effect, and the brightness of halo CMEs probably includes their driven (shock) waves.

We acknowledge that these previous studies have advanced our understanding of the white-light CMEs observed by coronagraphs, but it is not comprehensive. We also realize that there are few works identifying the source locations of all CMEs no matter whether the CME is halo or narrow, strong or faint. Most studies involving the information of source locations considered halo CMEs only [e.g., *Wang et al.*, 2002; *Zhou et al.*, 2003; *Zhao and Webb*, 2003]. Some others set certain criteria in the selection of CMEs. For example, the study by *Subramanian and Dere* [2001] only included the 32 CMEs with very clear EUV signatures on the solar surface. *Cremades and Bothmer* [2004] selected so called 'structured' CMEs, in which halo, narrow or faint CMEs are all excluded. *Yashiro et al.* [2005] work involved the CMEs associated with flares above C3 level. To our knowledge, the study by *Plunkett et al.* [2001], might be the only statistical work, in which all the CMEs during the period of interest, which is from 1997 April to December, were identified for their source locations.

An incomplete or biased sample may lead to unreliable or one-sided results, particularly, based on observations of coronagraphs, which have some intrinsic limitations. In this paper, we will identify the source locations of all the 1078 CMEs from 1997 to 1998 listed in the CDAW CME catalog¹ [*Yashiro et al.*, 2004], and try to better understand CMEs viewed in white-light coronagraphs. Except for the statistical results of CMEs' source locations, our investigation will address the following four issues.

1. *Missing rate of CMEs.* How many CMEs were missed

¹A widely-used manually-compiled catalog, refer to http://cdaw.gsfc.nasa.gov/CME_list/

by LASCO and EIT, and how many front-side CMEs were unnoticed by SOHO?

2. *Mass of CMEs.* Whether or not can the enhanced brightness in coronagraphs reflect the CME mass?
3. *Causes of halo CMEs.* Why do some CMEs manifest a halo appearance?
4. *Deflections of CMEs.* How often and significant are CMEs deflected in the corona and why?

The period of 1997 – 1998 is the beginning of the ascending phase of solar cycle 23, during which the solar condition is relatively simple and the solar activity level is low. Thus the source locations of CMEs are relatively easy to be identified with small ambiguity. This paper is organized as follows. In the next section, we present our data source, and particularly focus on the identification and classification of the CME source locations. The statistical results of the CME source locations are shown in Sec.3. In Sec.4, the four issues mention above are extensively discussed. A summary and conclusions are given in Sec.5.

2 Data Preparation

The CDAW CME catalog provides so far the most reliable list of CMEs recorded by SOHO/LASCO, in which some CME apparent parameters, such as angular width, position angle, linear speed, etc, are included. Since only the LASCO data are used by the catalog, there is no information of CMEs' source locations. To identify the source locations of CMEs, the SOHO/EIT 195 Å images are used. The identification method is similar to that employed by *Wang et al.* [2002], in which the time and propagation direction of a CME obtained from the LASCO movie is used to roughly locate the time and region of the CME in EIT 195 Å images and then this region is carefully checked if there is any EUV eruptive activity associated with the CME.

Lots of observations have suggested that various eruptive activities appearing at various wavelengths on the solar surface probably indicate the launch of a CME. These signatures could be flares in multiple wavelengths, dimmings and waves in EUV passbands, post-eruptive loops/arcades in X-ray and EUV images, etc. However, a CME process may not be accompanied with all of these phenomena. Flares are thought to be tightly related with CMEs [e.g., *Harrison*, 1995, 2003; *Zhang et al.*, 2001], but it has been statistically suggested that flares are not one-to-one associated with CMEs, vice versa [e.g., *St. Cyr and Webb*, 1991; *Wang et al.*, 2002; *Zhou et al.*, 2003; *Andrews*, 2003; *Yashiro et al.*, 2005; *Yermolaev and Yermolaev*, 2006]. A flare even stronger than X class could be associated without a CME [*Green et al.*, 2002; *Yashiro et al.*, 2005; *Wang and Zhang*, 2007]. A more confident solar surface signature of a CME is the combination of a flare and EUV dimming and/or waves. Thus, in our identification procedure, we assume that such a combined signature in EIT 195 Å images indicates a CME originating from visible solar disk.

Meanwhile, we realize that there is no conclusion that a front-side CME must be accompanied with some visible EUV signature on the solar surface, which was emphasized by *Yermolaev and Yermolaev* [2006] and *Yermolaev* [2008]. It

means that a CME without any eruptive signature in EIT 195 Å images might come from front-side solar disk. As will be discussed in Sec.4.1.3, such CMEs do exist. This has also been noted in the following classifications.

After a manually check of the EIT observations, the source locations of all the 1078 CMEs during 1997 – 1998 are identified. It is found that these CME source locations can be classified as the following four subsets.

1. *Location Identified (LI)*: For a CME in this subset, evident eruption features, such as brightening and/or dimming, on the solar disk seen in EIT 195 Å can be related to it. Such a CME definitely originated from the front-side of the Sun. Figure 1(a) and 1(b) show an example CME viewed in EIT and LASCO. From the EIT 195 Å image, we could assign a location (given in latitude and longitude) for the CME, which is usually the center of the eruption feature and the error is about 5 – 10 degrees. The measured location coordinates directly from EIT images are the apparent coordinates, but not in the heliographic coordinates. The heliographic coordinates can be calculated by applying the correction of the angle between the solar equatorial plane and ecliptic plane. According to each pair of the apparent coordinates, we can further derive the following two parameters. One is the projected distance of the source location from disk center (*DSC*) in the plane of sky. The other is the position angle of the source location (*SPA*). These two parameters are useful in the analysis of the projection effect, visibility and deflections of CMEs.

2. *Above Limb (AL)*: In this subset, we can only find eruption features associated with CMEs mainly above the solar limb as illustrated by the example shown in Figure 1(c) and 1(d). We could expect that these CMEs probably originated from the backside and were close to the limb of the Sun. For such a CME, the parameter *DSC* can not be obtained, but *SPA* could still be roughly estimated from the EIT images.

3. *No Signature (NS)*: No any eruption features were seen in the FOV of EIT for this subset of CMEs. Such CMEs probably originated from the backside of the Sun. Also it is possible that some of them launched from the front-side solar disk but had very weak signatures or originated at an altitude not corresponding to the EUV 195 Å passband.

4. *Poor Data (PD)*: The source locations of these CMEs can not be identified, because of low cadence, unqualified images and/or data gaps in EIT 195 Å data.

Table 1 lists the numbers of CMEs for the first three subsets. Except 231 PD CMEs that we have no sufficient data to identify their source regions, a total of 847 CMEs have been checked carefully, and it is found that there are 288 (occupying about 34%) CMEs with the source location at front-side solar disk, 234 (~ 28%) CMEs having been found above limb, and 325 (~ 38%) CMEs without any eruptive signatures in EUV 195 Å passband. Meanwhile, we give the confidence level (*CL*) of identification. Three levels are given. Level 1 means that the identification is confident; level 3 means ambiguous; and level 2 is between.

A list containing the information of the CMEs' source regions has been compiled at the website http://space.ustc.edu.cn/dreams/cme_sources/. Figure 2 is a glance of the list. For each CME, the list integrates the parameters from CDAW CME catalog (*CPA* and *MPA*, angular width, linear speed, etc.) and our own parameters (source location, *DSC*, *SPA*, *CL*, etc.). One

CL	1	2	3	Subtotal	Percentage
LI	189	60	39	288	34%
AL	160	60	14	234	28%
NS	214	92	19	325	38%
Total	563	212	72	847	100%

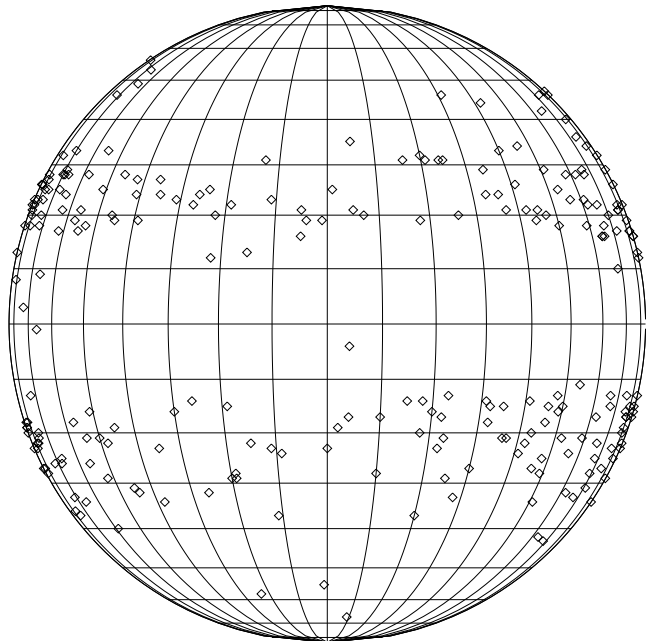


Figure 3: Distribution of the source locations of CMEs on a meshed solar disk.

can visit the website for more details. If not otherwise specified, in the following analysis, we only include the LI CMEs with *CL* equal to 1 and 2, which count the number of 249.

3 Statistical Results of Source Locations

3.1 Distribution of CME Source Locations

Figure 3 shows the distribution of the source locations of the LI CMEs. Some quick results could be obtained immediately. About 52%/48% of CMEs launched from northern/southern hemisphere, and about 54%/46% of CMEs originated from western/eastern hemisphere. Further, we consider a CME with *DSC* equal or larger than $0.85 R_S$ as a limb event (otherwise an on-disk event) and a CME with angular width larger than 100° as a halo event (otherwise a non-halo event). It is found that about 56% of CMEs come from solar limb (comparing with 44% of on-disk CMEs), and 18% of CMEs are halo (comparing with 82% of non-halo CMEs). Table 2 summarizes the numbers of the CMEs.

Figure 4(a) shows the distribution of the CMEs' source locations in latitude. The black line presents all the 249 CMEs, the red line is for the northern CMEs, and the blue line for southern CMEs. Note the numbers of the northern and southern CMEs are multiplied by a factor of 2 for clarity. Obviously, the distribution is south-north symmetrical and

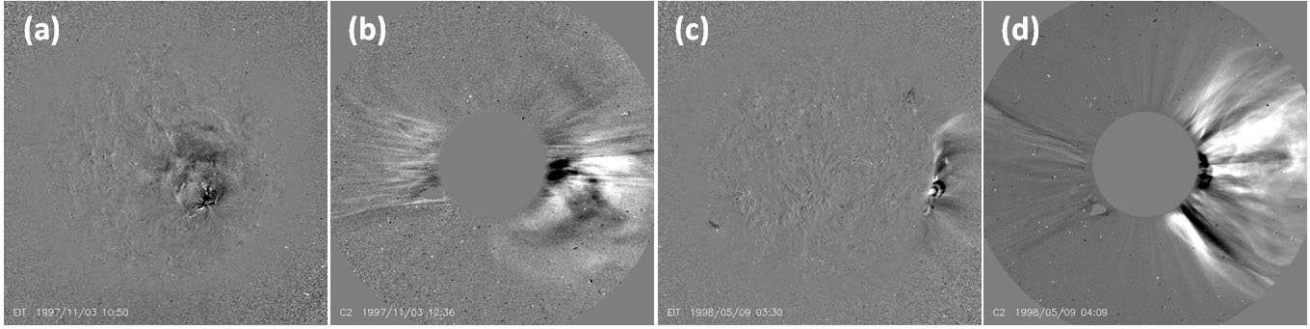



Figure 1: Panel (a) and (b) show the EIT and LASCO images of a LI CME on 1997 November 3. The CME's source location can be identified on the visible solar disk. Panel (c) and (d) show the same images of an AL CME on 1998 May 9, whose eruptive signature can only be seen above the west limb.



DREAMS
Data, REsearch & More in Space physics

Username
 Password

教育网用户可直接访问 <http://222.195.74.11/>

USTC-SPD | SLIPCAT | CMELOC | SHM | Feedbacks

[中文版](#) Location: [Homepage](#) >> [CMELOC](#)

CMEs in 1997 Oct [\(Back\)](#)

No.	First C2 Appearance UT	Location (Apparent Loc) deg	DSC Rs	SPA deg	CPA deg	MPA deg	Width deg	Speed km/s	Def	EIT Ref-Time UT	CL	Comment
1	1997/10/01 01:29:05	S33W67 (S35W69)	0.96	233.0	263	249	67	502	E	1997/10/01 00:49:09	1	
2	1997/10/01 16:27:05	N22E88 (N21E80)	0.99	68.1	91	93	20	187	E	1997/10/01 16:33:10	1	
3	1997/10/02 02:04:05	N20E81 (N19E76)	0.97	70.2	81	74	40	178	E	1997/10/02 01:12:31	1	

Figure 2: A snapshot of the web-based on-line list of CMEs. Visit http://space.ustc.edu.cn/dreams/cme_sources/ for details.

has a clear bimodal appearance with two outstanding peaks locating in $\pm(15^\circ - 30^\circ)$, respectively. The average latitude is $\sim \pm 24^\circ$, and it can be estimated that $\sim 71\%$ of CMEs originated from $\pm(15^\circ - 30^\circ)$. Moreover, there is no CME originating beyond $\pm 75^\circ$. The bimodal distribution is different from the distribution of CMEs' apparent latitudes measured in LASCO images, which is a distribution with only one peak near the solar equator [e.g., *St. Cyr et al.*, 2000; *Yashiro et al.*, 2004]. Such a difference was pointed out by *Plunkett et al.* [2001]. The reason why the distribution of the latitudes of source locations differs from that of the apparent latitudes could be (1) projection effect [*Hundhausen*, 1993], and (2) that most CMEs may not eject/propagate radially, but undergo an equator-ward deflection (refer to Sec.4.4). The first reason can be seen from the work by *Burkepile et al.* [2004], who studied the 111 limb CMEs observed by SMM and found a similar bimodal distribution of the CMEs' apparent latitudes with peaks at about $\pm 15^\circ$.

The longitude distribution of the CMEs' source locations

is presented in Figure 4(b). Similarly, there is no east-west asymmetry. The CME count is not uniformly distributed along the longitude, but increases with the increasing absolute longitude. The average longitude is $\sim \pm 54^\circ$, and about 49% of CMEs originated from the regions outside $\pm 60^\circ$. The non-uniform distribution of the longitude suggests that the CMEs originating from solar limb could be observed more easily than those near the disk center. The visibility of CMEs has been studied before [e.g., *Yashiro et al.*, 2005]. The three intrinsic limitations of coronagraph observations mentioned in the section of Introduction are responsible for such phenomenon. A more detailed discussion of the CME visibility or missing rate of CMEs will be given in the next section.

Combine the information of both latitude and longitude, we can get the distribution of CME counts with respect to the parameter *DSC*, as presented by the black histogram in Figure 5. It is found that the CME count increases dramatically as *DSC* increases. About 56% of CMEs took place

Table 2: Numbers of Different Kinds of LI CMEs

	Total	Northern	Southern	Western	Eastern	On-disk	Limb	Halo	Non-halo
Number	249	129	120	135	114	110	139	44	205
Percentage	100%	52%	48%	54%	46%	44%	56%	18%	82%

See the text for the definitions of the terms on-disk, limb, halo and non-halo.

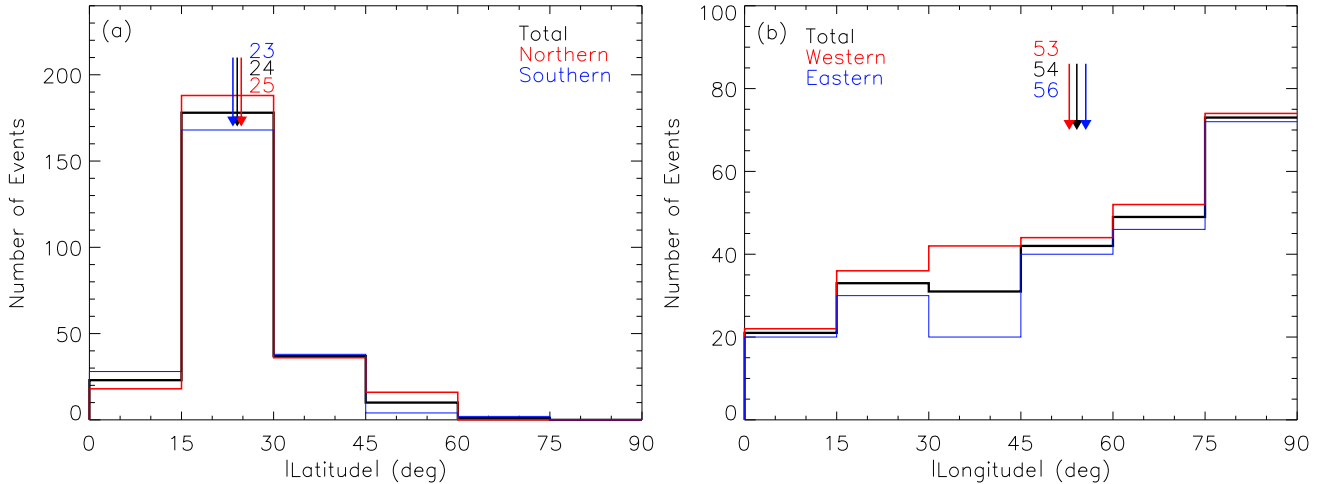


Figure 4: Histograms of the absolute values of the latitude and longitude for all CMEs and the CMEs in other two subsets (northern/southern for latitude and east/west for longitude). For clarity, the CME counts in the subsets are multiplied by a factor of 2. The color-coded arrows and numbers indicate the average values.

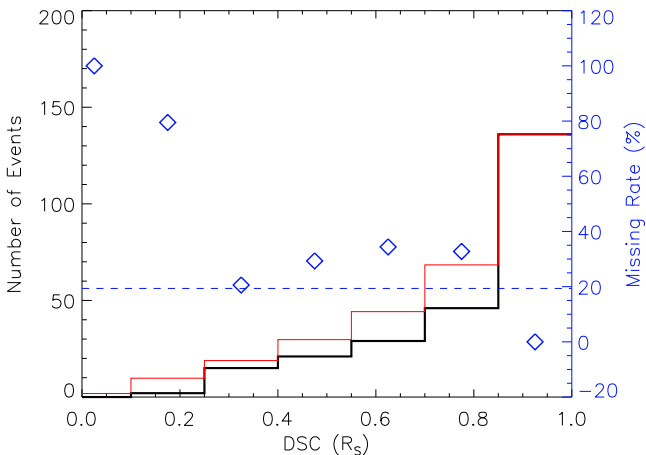


Figure 5: Histogram of DSC . The black one presents the observed CME counts, and the red one the expected CME counts. The missing rate of CMEs is given by the blue diamond symbols, which is measured by the vertical axis on the right. The dashed line marks the average missing rate. (See text for details)

outside of $DSC = 0.85R_S$, namely limb CMEs.

3.2 Correlations between CME Source Locations and Apparent Properties

Figure 6(a) and 6(b) display the scattering plot of the CME apparent speeds versus source locations, and the histograms of the speeds for limb, on-disk and all CMEs, respec-

tively. The both plots do not show any evident dependence of the speeds on the source locations. The speed histograms of limb, on-disk and all CMEs are quite similar. All of them have the same peak around $200 - 400 \text{ km s}^{-1}$ with the same average value of about 435 km s^{-1} . If the projection effect is taken into account, the on-disk CMEs should be generally faster than limb CMEs. This result is contrary to the study by *Burkepile et al.* [2004], who investigated 111 limb CMEs observed by SMM and found that their average apparent speed is 519 km s^{-1} , significantly larger than that of all SMM CMEs. They believe that the projection effect causes limb CMEs to have a greater apparent speed than other CMEs. However, according to our statistical result, we think that the selection bias in their study rather than the projection effect might be the real reason. The limb CMEs identified by them must be associated with a clear eruptive prominence or X-ray/ $H\alpha$ flare. The imposed criteria possibly made them filter out many weak/slow limb CMEs. This may also be the reason why their average speed of limb CMEs is larger than ours.

The distribution of angular width for all, limb and on-disk CMEs are shown in Figure 6(c) and 6(d). Although the scattering plot does not manifest any evident correlation between the width and position, the histograms for limb and on-disk CMEs are different. The average value of angular width is about 59° for limb CMEs, but 120° for on-disk CMEs. Moreover, almost all ($\sim 95\%$) of the full halo CMEs are on-disk CMEs. It suggests that the projection effect is significant for on-disk CMEs. A further discussion of the projection effect will be given in Sec.4.3. As the projection effect is minimized for limb CMEs, thus we think that the width distribution for limb CMEs obtained here reflects the

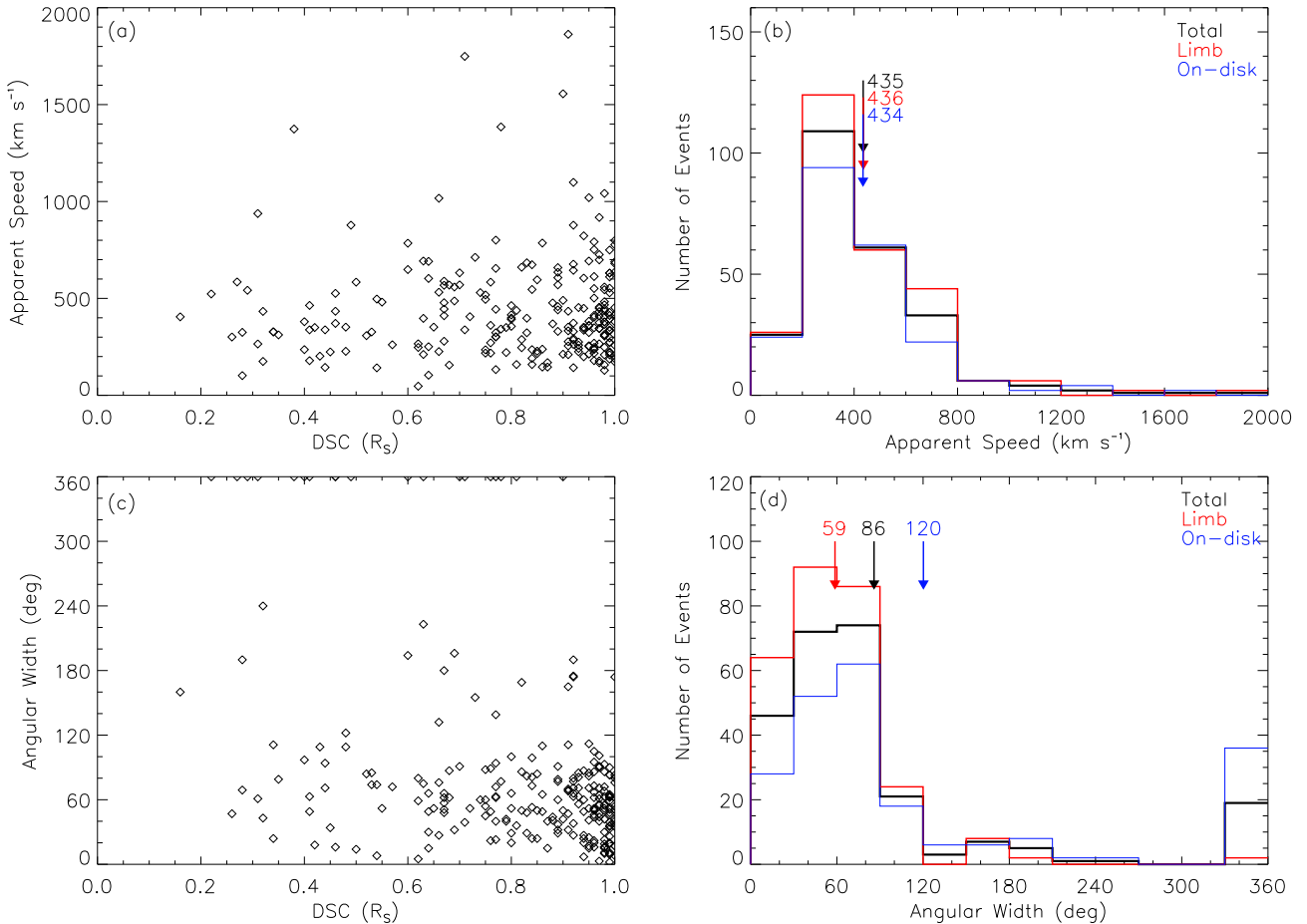


Figure 6: Panel (a) and (c) show the apparent speed and angular width, respectively, of CMEs as a function of DSC . Panel (b) and (d) present the histograms of the two parameters with the pattern as same as that in Figure 4.

truth. About 65% of limb CMEs have an angular width in the range of $30^\circ - 90^\circ$. The average angular width ($\sim 59^\circ$) of the limb CMEs is consistent with that ($\sim 47^\circ - 61^\circ$) obtained in previous work [e.g., *Burkepile et al., 2004; Yashiro et al., 2004*].

4 Inferences and Implications

The information of CMEs' source locations allows us to perform a deeper analysis than before. As has been mentioned in the section of Introduction, the following four issues will be addressed.

4.1 Missing Rate of CMEs

4.1.1 Visibility in EIT

First of all, it is known that not all of white-light CMEs could be seen in LASCO cameras. How many CMEs will be missed? Before answering this question, we will discuss the visibility of CMEs in EIT instrument. A primary function of EIT in CME study is to learn the eruptive processes of CMEs in corona. It is also a necessary tool to distinguish if a CME originates from front-side or back-side solar disk. This becomes even important when someone wants to predict the

geoeffectiveness of CMEs.

The comparison of the percentages of LI, AL and NS CMEs (Table 1), we found that there are a significant fraction of CMEs probably missed by EIT 195 \AA wavelength. It has been mentioned in Sec. 2 that AL CMEs are probably from backside disk but close to the limb. If all the NS CMEs are considered as backside events, the percentage of backside CMEs (NS + AL CMEs) would be about 66%, larger than the expected value 50%. It implies that a significant fraction, $\sim 16\%$, of LASCO CMEs probably occurred on the front-side solar disk, but did not leave any visible eruptive signatures in EIT 195 \AA images.

Further, the speed histograms in Figure 6(b) suggests that there is a jump around 200 km s^{-1} . The CMEs with speed less than 200 km s^{-1} occupy about ten percent only, and particularly, there is only one CME slower than 100 km s^{-1} . However, the statistical analysis of all LASCO CMEs did not show such a speed cut-off at low value (refer to Figure 4 in *St. Cyr et al. 2000* and Figure 5 in *Yashiro et al. 2004*). Consider that our sample includes LI CMEs only, thus the low rate of slow CMEs we obtained here probably reflects the fact that there is a threshold of speed somewhere between 100 and 200 km s^{-1} , and a CME with a speed less than the threshold is generally too weak to leave an evident eruptive signature on the solar surface.

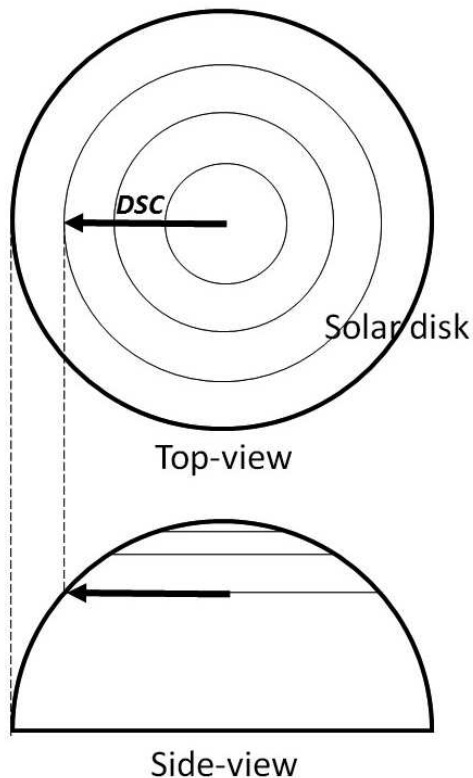


Figure 7: A schematic picture illustrates the effect of the spherical geometry on the CME distribution with DSC .

4.1.2 Visibility in LASCO

To address the visibility of CMEs in LASCO, we have to make two assumptions. The first one is that the limb CMEs are all visible to LASCO. This assumption is reasonable because limb CMEs are supposed to be least affected by projection effect, occulting effect and Thomson scattering effect. Also this assumption seems to be true according to *Yashiro et al.* [2005] work. The second assumption is that all the 16% front-side CMEs missed by EIT have the source location distribution as same as the LI CMEs. Then the above question may be answered by studying the DSC distribution of LI CMEs shown in Figure 5.

If CMEs uniform-randomly occur on the solar surface and all of them can be detected, the spherical geometry will cause a non-uniform distribution of the CME occurrence rate with respect to DSC , as illustrated by Figure 7. It is easily obtained that the contribution of the spherical geometry to the probability distribution of the CME counts is given by

$$P = \begin{cases} A \frac{2\pi DSC}{\sqrt{1-DSC^2}} \left[1 - \frac{2}{\pi} \arccos\left(\frac{\sin 60^\circ}{DSC}\right) \right], & DSC > \sin 60^\circ \\ A \frac{2\pi DSC}{\sqrt{1-DSC^2}}, & DSC \leq \sin 60^\circ \end{cases} \quad (1)$$

in which the coefficient $A \approx 0.2$ makes the integration of P over DSC is unity. Here $\sin 60^\circ$ corresponds to the latitude of $\pm 60^\circ$. This threshold must be set because there are few CMEs originating from the high latitude regions (refer to Fig.3). Under the assumption that all limb CMEs are visible to LASCO, the expected CME counts in each DSC bin can

be calculated by Eq.1, which has been presented by the red histogram in Figure 5.

Comparing the red and black histograms, we are able to estimate the missing rate of CMEs for SOHO/LASCO, which is given by the following formula

$$\text{Missing Rate} = \frac{\text{Expected CME Counts} - \text{Recorded CME Counts}}{\text{Expected CME Counts}} \quad (2)$$

The blue symbols in Figure 5 indicate the missing rate. It is found that the missing rate roughly decreases with increasing DSC , and on average, about 19% of CMEs are not detected by the coronagraph. This missing rate is slightly larger than that obtained by *Yashiro et al.* [2005], who investigated the CME association of X-ray flares greater than C3 and found a missing rate of $\sim 14\%$ averagely. In their statistics, the missing rate increases as the associated flare intensity decreases. Thus, their missing rate should be slightly underestimated, because they did not consider flares weaker than C3.

4.1.3 Invisible Front-side CMEs

Combining the missing rates of white-light CMEs in LASCO and front-side CMEs in EIT, we may infer that about 32% of front-side CMEs can not be recognized by SOHO. Recently, a concept of ‘stealth’ CMEs has been proposed to describe a kind of CMEs that do not leave any eruptive signatures in EUV passbands and sometimes may not even be visible in coronagraphs facing on them. The observations from STEREO twin spacecraft did support the existence of such cases, like the 2008 June 1 event [*Robbrecht et al.*, 2009]. This event totally had no eruptive signature in STEREO/EUVI images and was extremely faint in the coronagraphs on board STEREO-B. If there was no STEREO-A spacecraft, in which the CME was a limb event, it would probably be missed. Here we call these 32% of front-side CMEs ‘SOHO stealth’ CMEs.

Frankly, the rate sounds too high, because there are only several cases found in STEREO data. This is probably caused by some technique limits of SOHO. For example, the cadence of SOHO/EIT is 12 minutes, and therefore, a quick eruption lasting less than 12 minutes is possible to be missed by EIT. Besides, low signal-to-noise ratio is another possible technique reason. Of course, there is a physical explanation that such a stealth CME might launch from an altitude not corresponding to the designed EUV passbands of instruments, so that no signature can be observed. No matter which reason is, it is clear that these stealth CMEs should be weak and probably travel across a relatively small region on the solar surface.

The 32% SOHO stealth CMEs provide us a reasonable explanation of the high rate of the missing alert of geomagnetic storms and/or ICMEs encountering the Earth. The association of ICMEs with CMEs has been studied by many researchers before [e.g., *Lindsay et al.*, 1999; *Cane et al.*, 2000; *Gopalswamy et al.*, 2000b; *Cane and Richardson*, 2003], and was summarized in the review by *Yermolaev and Yermolaev* [2006]. A fact revealed by these investigations is that the association rate is not 100%, and about 18 – 44% of ICMEs can not be found the corresponding CMEs. The missing rate obtained from our study is in highly agreement with these previous results.

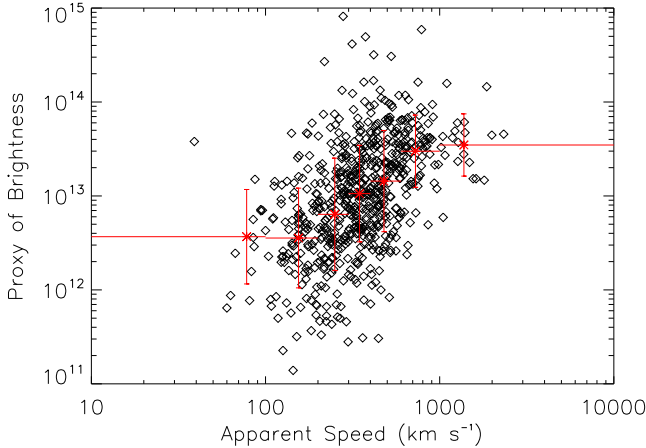


Figure 8: The scattering plot of the CME brightness proxy versus the apparent speed for the CMEs from 1997 to 1998. The red symbols with error bars mark the average value of the brightness proxy within the speed range indicated by the associated horizontal red lines.

A direct consequence is that there would be a significant fraction of geomagnetic storms are probably not able to be predicted. *Webb et al.* [1998] in their paper discussed so-called first ‘problem’ storm, the 1997 January 17 event. This event was thought no CME was observed to associate with, though the interplanetary shock ejecta pair causing this storm was obvious. There are many other problem storms, which can be found in the studies by, e.g., *Webb et al.* [2000], *Schwenn et al.* [2005], and *Zhang et al.* [2007]. The existence of stealth CMEs is a natural explanation of such storms. There are also other explanations. One is the longitudinal extension of CMEs [*Webb et al.*, 2000; *Zhang et al.*, 2003], and the other is the CME deflections [*Wang et al.*, 2004, 2006]. The latter will be discussed further in Sec.4.4.

4.2 Mass of CMEs

The previous studies suggested that the mass of a typical CME is about 10^{12} kg [e.g., *Vourlidas et al.*, 2000]. The value is estimated according to the brightness of the transient structure detected in coronagraphs. Actually the enhanced brightness is not only contributed by the CME, but also the compressed solar wind plasma surrounding the CME. Before discussing this issue, we must clarify the definition of CME. The CME was first observed by the white-light coronagraph onboard OSO-7 in December 1971, and defined as an enhanced bright erupting structure, i.e., the luminescence area in the FOV of a coronagraph. However, this graphic definition is not strict, because ambient solar wind plasma may be disrupted by a CME and caused brightened. Thus, here a CME strictly refers to the plasma ejected away from the solar atmosphere that does not include the disrupted solar wind. As to the luminescence area in the FOV of a coronagraph during a CME, we call it transient. What we will study below is whether or not the transient contains only the CME.

There is the parameter of mass listed in CDAW CME catalog. The mass is estimated by the method developed by *Vourlidas et al.* [2000] based on observations of white-light

coronagraphs and some assumptions. Briefly, the estimated mass of a transient is the product of the size of the luminescence region and the value of the enhanced brightness. Angular width is an important parameter to weight the size of the region though we do not have the information of the span of the region along the radial direction. Thus, as a first-order approximation, we may derive a new parameter, which is the ratio of the mass to the angular width, and treat it as a proxy of the brightness of a transient. Figure 8 presents the brightness proxy versus the apparent speed, in which all the CMEs listed in the CDAW CME catalog during 1997 – 1998 are included. Surprisingly, there is an obvious positive correlation between the two parameters. Actually, this phenomenon has been implied in Figure 6(b), which shows that the distributions of speeds for limb and on-disk CMEs are quite similar. It should be pointed, however, that the correlation coefficient is only 0.5 and the scattering is significant. We think that such large scattering may be due to the inaccurately estimation of the mass, angular width, etc. Overall, there is a trend that transients with a slower apparent speed look fainter in a coronagraph.

Let’s compare two identical transients with the same apparent speed. Transient-1 rises above the limb and Transient-2 comes from the longitude of 30° and equator. The two transients should have the same brightness according to the above analysis, but the real speed and heliocentric distance of Transient-2 should be twice as large as those of Transient-1 if the projection effect is taken into account. So tracking Transient-2 back to the heliocentric distance of Transient-1, its brightness should be doubled. By assuming that the speed of the transient changes little within that region, it can be inferred that the brightness of a transient at any given heliocentric distance should be positively correlated with its real speed.

Why is the brightness of a transient controlled by its speed? It can be easily explained if a transient contains not only a CME but also the ambient compressed solar wind plasma due to the CME. The faster a CME is, the greater is compression of the ambient solar wind plasma, and therefore the brighter the transient looks. This picture confirms and deepens the previous thought of three-component-structure CMEs that the bright fronts of CMEs are believed to be the compressed solar wind. Our result obtained here is suitable for any type CMEs. Thus, the mass given in the CDAW CME catalog is not merely the CME mass, but the mass of both the CME and the ambient compressed solar wind plasma, which we can call it ‘apparent mass’.

To a certain extent, the mass component contributed by the compressed solar wind plasma stands for the ‘virtual’ mass, which is a concept first proposed in fluid mechanics. Briefly, the presence of virtual mass is because ‘an accelerating or decelerating body must move some volume of surrounding fluid as it moves through it, since the object and fluid cannot occupy the same physical space simultaneously².’ Since CMEs propagate in solar wind, the concept of virtual mass is also applicable to the CME studies. In practice, the apparent mass is obtainable, but not the CME mass or virtual mass, and scientists are used to using the apparent mass as the CME mass. In that situation, the CME mass is overestimated, and the CME volume is obviously

²Adapted from Wikipedia http://en.wikipedia.org/wiki/Added_mass

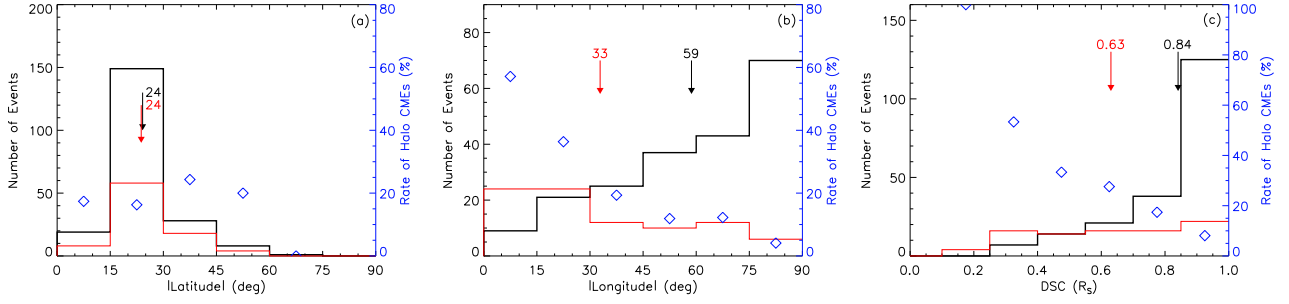


Figure 9: The histograms of absolute value of latitude (panel a), absolute value of longitude (panel b) and DSC (panel c) for halo (red) and non-halo CMEs (black), respectively. The blue diamond symbols denote the rate of halo CMEs. For clarity, the counts of halo CMEs are multiplied by a factor of 2.

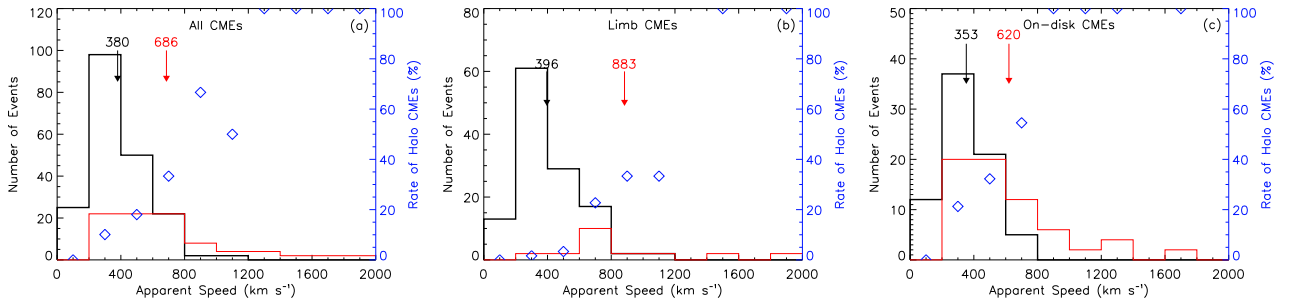


Figure 10: From (a) to (c), the panels show the histograms of apparent speed for all, limb and on-disk CMEs, respectively. The pattern of them is as the same as that in Figure 9.

also overestimated. These overestimations will lead to uncertainties or errors in other relevant CME studies, e.g., the CME trigger and initiation, the CME aerodynamics in IP space. If we can not accurately estimate the kinetic energy of a CME, we may not really understand how a CME energy is accumulated and released. If we do not know the volume and mass of a CME precisely, we may add a wrong virtual mass in the governing equation of CME aerodynamics and also may be difficult to figure out how large the drag force acting on a CME is when it propagates in corona and interplanetary space (previous researches can be found in, e.g., *Cargill et al. 1996; Cargill 2004*). Some deeper discussions about these issues are worthy of being pursued in another paper.

4.3 Causes of Halo CMEs

Halo CMEs generally get special attention of many researchers as they have a higher probability to hit the Earth. This is because people believe that the projection effect is the main cause of a CME looking halo. However, it is not the only cause. This point can be seen by comparing the distributions of halo and non-halo CMEs.

4.3.1 Halo vs. Non-halo CMEs

As has been defined before, we consider a CME to be halo when its apparent angular width is larger than 100° , otherwise the CME is non-halo one. The numbers of halo and non-halo CMEs have been listed in Table 2. The similarity and difference between the two kinds of CMEs in the distribution of source locations are given in Figure 9. The

latitude distributions of halo and non-halo CMEs are similar to each other (Fig.9(a)), and both of them have a peak at around $\pm(15^\circ - 30^\circ)$. The rate of halo CMEs, i.e., the ratio of the number of halo CMEs to the number of all CMEs (indicated by the blue symbols), is around 20%. The longitude distributions of them are quite different (Fig.9(b)). For halo CMEs, the average longitude is about 33° , and the CME count decreases as the absolute value of longitude increases; whereas for non-halo CMEs, the average longitude is about 59° , and the count increases. It could be found that the longitude distribution of halo CMEs is relatively flat comparing to that of non-halo CMEs. The rate of halo CMEs has a clear decrease trend from central meridian to limb. Within $\pm 15^\circ$, the rate reaches $\sim 57\%$, while outside of $\pm 75^\circ$ the rate is as low as $\sim 4\%$.

As did before, we further investigate the parameter DSC , which is shown in Figure 9(c). The distributions of the two kinds of CMEs present a substantial difference. Most non-halo CMEs come from the regions far away from the disk center. It can be estimated that there are about 62% of non-halo CMEs with DSC equal or larger than $0.85 R_S$, and no non-halo CME originating from central region with DSC less than $0.25 R_S$. On contrary, the distribution of halo CMEs is much flatter, indicating that halo CMEs could originate anywhere. The rate of halo CMEs monotonically decreases from 100% to $\sim 8\%$ with the increasing DSC . However, one may notice that the highest peak of the distribution of halo CMEs appears in the DSC range of $0.85 - 1.0 R_S$, which occupies 25% of the halo CMEs. These results imply that (1) projection effect is indeed one factor causing a CME looking halo, but (2) it is not the only one factor, especially for

those halo CMEs close to the solar limb. As will be seen below, the ‘violent eruption’ probably is the other major cause. The term ‘violent eruption’ here means an eruptive process, during which the released energy is higher than usual and the release process is quicker.

Lara *et al.* [2006] had exclusively addressed the issue whether or not halo CMEs are special events, and reached the conclusion that the behavior of halo CMEs can not be explained merely by projection effect. They believe that ‘the observed halo is the manifestation of the shock wave driven by fast CMEs’. To drive a shock wave, the CME speed must be larger than local Alfvénic speed, i.e., halo CMEs should be much energetic. Thus, their interpretation on halo CMEs is more or less consistent with our second point of view given in the last paragraph. Moreover, that point can be further clarified by the comparison of the speed distributions among the halo/non-halo and on-disk/limb CMEs.

4.3.2 Limb vs. On-disk CMEs

Figure 10(a) suggests that the average speed of halo CMEs is generally twice as large as that of non-halo CMEs. Moreover, for CMEs with speed $\leq 800 \text{ km s}^{-1}$, the rate of halo CMEs is about 14%, while, for CMEs with speed $> 800 \text{ km s}^{-1}$, the rate jumps to $\sim 73\%$, and these fast halo CMEs occupies about 25% of all halo ones. Particularly, all the five CMEs with speed larger than 1200 km s^{-1} are halo. Since there are few non-halo CMEs faster than 800 km s^{-1} , the percentage 25% roughly indicates how many halo CMEs are faster, i.e., more energetic, than the average level of CMEs.

To reduce the projection effect in our analysis, we investigate the limb and on-disk CMEs separately. Figure 10(b) is for limb CMEs, in which the halo CMEs occupy a percentage of $\sim 8\%$. It is evident that the distributions of halo and non-halo CMEs are much different. The peak of the distribution of halo CMEs locates between $600 - 800 \text{ km s}^{-1}$ with the average value of about 883 km s^{-1} , and about 36% of halo CMEs have an apparent speed larger than 800 km s^{-1} . On the contrary, the peak of non-halo CMEs is between $200 - 400 \text{ km s}^{-1}$ with the average value of 396 km s^{-1} , and only about 3% of them are faster than 800 km s^{-1} . Thus, we think that the violent eruption is the dominant reason for a limb CME to be halo.

For on-disk CMEs (Fig.10(c)), in which there are about 30% halo CMEs, the average speed of halo CMEs (620 km s^{-1}) is also nearly twice of that of non-halo CMEs (353 km s^{-1}). All the on-disk CMEs with an apparent speed larger than 800 km s^{-1} are halo ones, which occupies about 21% of the entire on-disk halo CMEs. These results suggest that the violent eruption is at least one of the major causes of halo CMEs. On the other hand, comparing Figure 10(b) and 10(c), we find that the histograms of on-disk and limb non-halo CMEs are similar, while the histogram of on-disk halo CMEs is quite different from that of limb halo CMEs. For limb CMEs, most halo CMEs are faster than 600 km s^{-1} . However, for on-disk CMEs, most halo CMEs are slower than 600 km s^{-1} , which indicates that projection effect is still a non-ignorable factor leading an on-disk CME to have a halo appearance.

In summary, both projection effect and violent eruption are the major causes of halo CMEs. The projection effect being a cause is because (1) the rate of halo CMEs monotonically

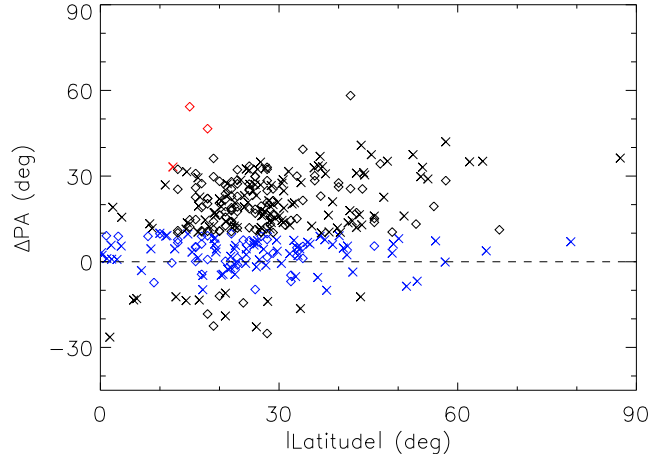


Figure 11: A scattering plot showing the deflection angle as a function of the absolute latitude of the CME source location. A data point above the dashed line at zero means the CME deflected towards equator, otherwise towards polar regions. The blue symbols mark the events with deflection angle less than 10° , which we treated as radial events. The red symbols mark the events, whose deflection crosses over the equator by more than 20° .

decreases from 100% to 8% as the CME source location moves from disk center to limb, (2) no non-halo CMEs originated from the regions with $DSC < 0.25R_S$, and (3) the average angular width of on-disk CMEs is $\sim 120^\circ$, twice of that of limb CMEs, and about 95% of full halo CMEs are on-disk CMEs. The second cause can be seen from the following facts. (1) About 25% of halo CMEs originating from solar limb ($DSC \geq 0.85R_S$), where the projection effect is minimized. (2) The apparent speed of halo CMEs is average twice of that of non-halo CMEs, no matter whether they are on-disk or limb CMEs. (3) Most of fast CMEs are halo CMEs; especially the rate is 100% for speed $> 1200 \text{ km s}^{-1}$. Besides, for limb halo CMEs, the violent eruption is the primary cause. Overall, there are about 25% of halo CMEs above the average level of CME energy.

4.4 Deflections of CMEs

4.4.1 Statistical Results and Classification

In our dataset, we have the parameter SPA (measured in EIT images) of LI and AL CMEs, and therefore the deflections of CMEs can be studied by comparing SPA with the central position angles (CPA , measured in LASCO) of CMEs. To reduce the projection effect, only the 138 limb LI CMEs and 191 non-halo AL CMEs with available position angles and CL equal to 1 and 2 are considered. To obtain the direction and magnitude of the deflection of these CMEs, we calculate the difference (ΔPA) between SPA and CPA . Figure 11 presents ΔPA as a function of the absolute latitude of CME’s source location. LI CMEs are denoted by diamonds, and AL CMEs by ‘x’. Note that, for AL CMEs, we use SPA to estimate the approximate latitudes of their source locations, as we believe that these CMEs occurred near the solar limb though they were on the backside. A positive value of ΔPA means an equator-ward deflection

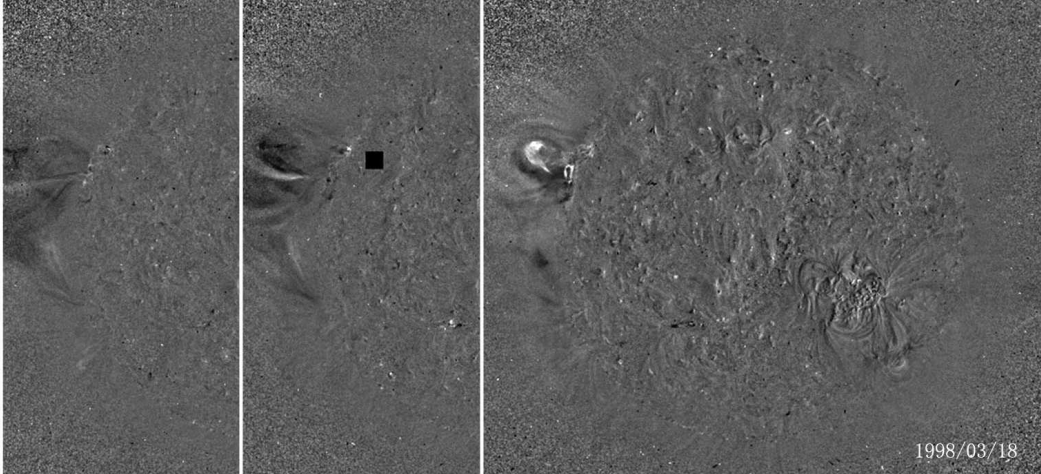


Figure 12: Asymmetrical expansion of a CME on 1998 March 18, which resulted in the significant difference between SPA and CPA .

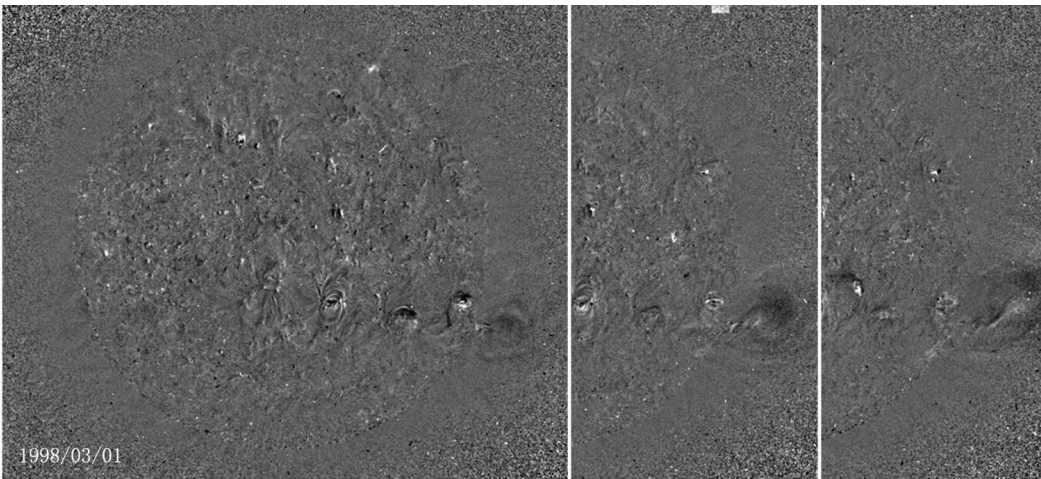


Figure 13: Non-radial ejection of a CME on 1998 March 1.

while a negative value corresponds to a pole-ward deflection. Considering the error in determining the CME's source location and CPA , we treat the CMEs with $|\Delta PA| < 10^\circ$ as radial events (the blue symbols in the figure).

From Figure 11, it is obtained straightforwardly that (1) about 62% of CMEs underwent an equator-ward deflection with the average deflection angle of $\sim 22^\circ$, (2) about 5% of CMEs manifested a significant pole-ward deflection with the average angle of $\sim 16^\circ$, and (3) at high latitude regions (outside of $\pm 45^\circ$), most (21 out of 31) CMEs deflected towards equator and no CME towards the polar region.

Note that the deflections obtained here is simply from the comparison of the position angle of the CME eruptive signature in EIT FOV and the CME central position angle in LASCO FOV. Any measurement errors and inconsistency between the two measurements will result in a faked deflection. For many CMEs, the errors of the coordinates of their source locations are about 10 degrees, which have been considered in the above analysis. However, CMEs are a large scale structure. Their source regions may span over a large area, and the identified source locations in EIT images may possibly be not centered beneath CMEs [e.g., *Harrison,*

1995; *Harrison and Lyons,* 2000; *Plunkett et al.,* 2001]. A quick check of the EIT movies, we find that some CMEs do have two widely separated footpoints, and the identified source locations (i.e., the most significant eruptive features) are close to one of them, e.g., the 1998 April 20 and 1998 December 7 CMEs. For such cases, the derived ΔPA are probably not correct or suffer a much larger error.

Although the faked deflections do exist, most deflections of CMEs in our statistics are true. We find that these deflection behaviors can be classified into three types. The first type is the manifestation of *asymmetrical expansion* of CMEs. As a case, Figure 12 shows the EIT images of the CME on 1998 March 18. At the beginning, there was a clear flux-rope structure standing right-up on the eastern limb. As the eruption progressed, the CME flux rope expanded asymmetrically. Its boundary close to the equator was freely expanding, but the expansion of the boundary close to the pole was obviously blocked by something. This asymmetrical expansion caused the CME deflecting to the equator. The second type is the *non-radial ejection*. The CME occurring on 1998 March 1 belongs to this type, as shown in Figure 13. The CME flux rope was inclined toward equa-

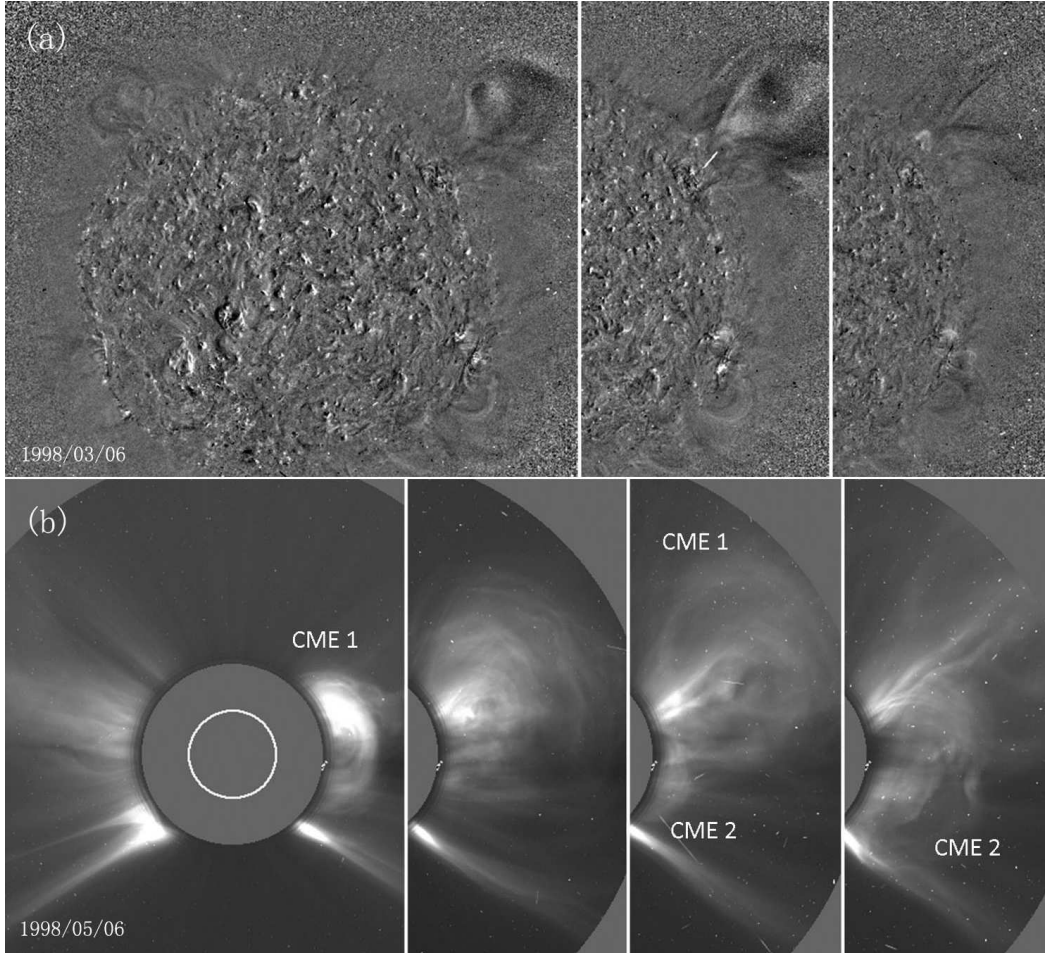


Figure 14: Panel (a): Curved propagation of a CME viewed in FOV of EIT on 1998 March 6. Panel (b): Deflected propagation of a CME (CME1) viewed in FOV of LASCO on 1998 May 6, which is caused by the collision of CME1 with a following CME (CME2).

tor before the eruption, i.e., the direction of its ejection is non-radial initially. Such configuration of the CME naturally leads to a non-radial propagation after the non-radial ejection. The last type is called *deflected propagation*. Not like the second type, this type of deflections is mainly due to the interaction of CMEs with other neighboring structures during their propagation in the corona. The neighboring structures could be either the magnetic fields from coronal holes or other CMEs. For example, Figure 14(a) presents a CME on the western limb on 1998 March 6, whose trajectory in the FOV of EIT is curved. Apparently, the curved propagation of the CME is due to the presence of the polar magnetic field. The deflections caused by the interaction between CMEs is demonstrated in Figure 14(b). The CME (labeled as CME1), to be deflected, appeared above the western limb in the FOV of LASCO on 1998 May 6, and initially propagated along the position angle of $\sim 270^\circ$. However, its trajectory was quickly deflected toward the north pole due to the collision of the CME with a following CME (labeled as CME2). The collision of CMEs causing CME deflections was reported by *Gopalswamy et al.* [2001], and also studied with numerical simulations by *Xiong et al.* [2006, 2009].

4.4.2 Interpretation and Exceptions

Except the deflections caused by interactions of CMEs, which is not frequent during the solar minimum, almost all the CME deflections are essentially due to the pre-existing magnetic field structures surrounding the CMEs. For asymmetrical expansions and deflected propagations, the presence of the ambient coronal magnetic field and solar wind originating from the neighboring coronal holes may play a major role [e.g., *Gopalswamy et al.*, 2004], while for non-radial ejections, the magnetic field configuration in CME source regions decides the CME launch directions. Near the solar minimum, the Sun has an approximately dipole field, coronal holes usually appear in the polar regions, from which the magnetic field and solar wind super-radially disperse towards the equator, and therefore CMEs are deflected. This picture is in agreement with the statistical result obtained here that most CMEs propagated towards the equator. A model based on the distribution of coronal magnetic energy density has been proposed to quantitatively describe the CME's deflection in corona [*Shen et al.*, 2010], which points out that a CME will be deflected towards a place with a lower energy density.

One may notice that there are some cross-equatorial de-

Table 3: Event List of Unusual Deflections

No.	Date Time	Location	SPA	CPA	ΔPA	Width	Speed
	UT		deg	deg	deg	deg	km s ⁻¹
Pole-ward Deflection							
P1	1998/11/25 06:30:05	N18 E72	71	53	-18	41	256
P2	1998/11/25 14:30:05	N20 E73	69	57	-12	52	213
P3	1998/11/26 11:30:06	N19 E57	68	45	-23	50	216
P4	1998/12/04 21:30:10	S24 W56	241	227	-14	65	238
P5	1998/12/07 15:30:05	N28 W62	302	327	-25	42	490
P6	1998/02/24 18:27:05	-	264	251	-13	43	259
P7	1998/03/17 15:06:15	-	134	146	-12	6	204
P8	1998/05/09 15:18:25	-	242	228	-14	46	533
P9	1998/05/30 23:28:13	-	264	251	-13	63	594
P10	1998/06/02 21:06:24	-	69	50	-19	61	782
P11	1998/06/17 06:55:18	-	284	298	-14	23	632
P12	1998/10/28 04:54:05	-	56	40	-16	59	208
P13	1998/10/28 07:54:05	-	107	120	-13	66	486
P14	1998/11/01 08:18:09	-	291	302	-11	25	238
P15	1998/11/10 01:54:05	-	257	245	-12	29	284
P16	1998/11/12 05:54:06	-	244	221	-23	19	254
P17	1998/12/06 10:54:05	-	92	118	-26	73	806
Equator-ward Overshooting							
O1	1998/03/18 07:33:06	N18 E87	71	118	47	174	636
O2	1998/05/06 08:29:13	S15 W67	255	309	54	190	1099
O3	1998/06/15 06:55:20	-	258	291	33	93	535

The CMEs without identified locations are the AL events.

deflections (the red symbols in Fig.11) and pole-ward deflections, which have been listed in Table 3. Here the cross-equatorial deflection is defined for the CMEs with $\Delta PA - |\text{Latitude}| > 20^\circ$, which we also called equator-ward overshooting. The two kinds of deflections are not expected according to the above analysis. A question is naturally raised whether these unusual deflections are exceptional cases, or they can also be described by the same model. According to the parameters listed in Table 3, a quick impression can be established for limb LI CMEs that all the pole-ward deflections happened to narrow and slow CMEs, while all the equator-ward overshootings were associated with wide and fast CMEs. The same trend seemingly applies to AL CMEs. A further detailed study of all the deflected CMEs including these unusual events will be pursued in another paper.

5 Concluding Remarks

By manually checking the LASCO and EIT movies of all the 1078 CMEs listed in CDAW CME catalog during 1997 – 1998, the solar surface sources of these CMEs are identified, and a web-based on-line list of them with the information of their source locations is established at http://space.ustc.edu.cn/dreams/cme_sources. The

source locations and apparent properties of CMEs have the following features.

The distribution of CME source locations in latitude manifests a clear bimodal appearance with two most probable peaks in $\pm(15^\circ - 30^\circ)$, which is consistent with the location of active region belt. No CMEs came from polar regions (outside of $\pm 75^\circ$). About 56% of detected CMEs occurred near the solar limb (refer to Sec.3.1). The average apparent speed of CMEs is about 435 km s^{-1} , and there is no evident difference between the apparent speeds of on-disk and limb CMEs. According to the analysis of limb CMEs, the average value of angular widths of CMEs is about 59° , and about 65% of them have a width from 30° to 90° . Generally, on-disk CMEs are twice wider than limb CMEs, which suggests a significant projection effect (refer to Sec.3.2).

Further, through the analysis based on the source locations of all CMEs, we infer many interesting results.

1. About 16% of LASCO CMEs probably originated from front-side solar disk but left no evident eruptive signatures in the FOV of EIT, and a lower cut-off for the CME visibility in EIT, which corresponds to the apparent speed range of $100 - 200 \text{ km s}^{-1}$, probably exists. (Sec.4.1.1)
2. About 19% of CMEs were not detected by LASCO, and the missing rate has a trend to monotonically increase as the CME source location moves from limb to disk center. (Sec.4.1.2)
3. About 32% of front-side CMEs can not be recognized by SOHO, which becomes a natural explanation of high rate of missing alert of geomagnetic storms and is also in agreement with the previous results that about 18 – 44% of ICMEs do not have the corresponding CMEs. (Sec.4.1.3)
4. The brightness of a white-light CME at any heliocentric distance is roughly positively-correlated with its speed, which implies that (1) a bright transient recorded in white-light coronagraphs is contributed by both a CME and the compressed solar wind plasma surrounding the CME, and (2) the CME mass derived from the brightness is probably overestimated. (Sec.4.2)
5. Both projection effect and violent eruption are the major causes of halo CMEs, but for limb halo CMEs, the latter should be the primary one. Overall, there are about 25% of halo CMEs stronger than the average level of CMEs. (Sec.4.3)
6. Most CMEs manifest deflection behaviors near the solar minimum. About 62% of CMEs underwent an equator-ward deflection with the average deflection angle of $\sim 22^\circ$, and about 5% of CMEs had a significant pole-ward deflection with the average angle of $\sim 16^\circ$. At high latitude regions (outside of $\pm 45^\circ$), most CMEs deflected towards equator. (Sec.4.4)
7. The CME deflections can be classified into three types. One is due to the asymmetrical expansion, one is the non-radial ejection, and the other is the deflected propagation caused by the interaction of the CME with other neighboring magnetic field structures. (Sec.4.4.1)

These findings help people understanding the CMEs viewed in white-light coronagraphs more properly and precisely. We believe that some new and deeper questions have emerged from these results. This paper presents our first work established on the information of CME source locations, and gives us the overview of white-light CMEs. In our follow-up works, we will continue to address issues, e.g., the CME deflections, the role of active regions in producing CMEs, the relationship of CMEs with flares, etc.

Acknowledgments. We acknowledge the use of the data from the CDAW CME catalog, which is generated and maintained at the CDAW Data Center by NASA and The Catholic University of America in cooperation with the Naval Research Laboratory. SOHO is a project of international cooperation between ESA and NASA. We thank J. Zhang at George Mason University for his advice in identifying CMEs' source locations. This research is supported by grants from 973 key project 2011CB811403, NSFC 40525014, 40874075, 40904046, FANEDD 200530, CAS KZCX2-YW-QN511, 100-Talent Program of CAS, and the fundamental research funds for the central universities.

References

- Andrews, M. D., The front-to-back asymmetry of coronal emission, *Sol. Phys.*, *208*, 317–324, 2002.
- Andrews, M. D., A search for CMEs associated with big flares, *Sol. Phys.*, *218*, 261–279, 2003.
- Burkepile, J. T., A. J. Hundhausen, A. L. Stanger, O. C. St. Cyr, and J. A. Seiden, Role of projection effects on solar coronal mass ejection properties: 1. a study of CMEs associated with limb activity, *J. Geophys. Res.*, *109*(A3), A03,103, 2004.
- Cane, H. V., and I. G. Richardson, Interplanetary coronal mass ejections in the near-earth solar wind during 1996–2002, *J. Geophys. Res.*, *108*(A4), 1156, doi:10.1029/2002JA009,817, 2003.
- Cane, H. V., I. G. Richardson, and O. C. St. Cyr, Coronal mass ejections, interplanetary ejecta and geomagnetic storms, *Geophys. Res. Lett.*, *27*, 3591–3594, 2000.
- Cargill, P. J., On the aerodynamic drag force acting on interplanetary coronal mass ejections, *Sol. Phys.*, *221*, 135–149, 2004.
- Cargill, P. J., J. Chen, D. S. Spicer, and S. T. Zalesak, Magnetohydrodynamic simulations of the motion of magnetic flux tubes through a magnetized plasma, *J. Geophys. Res.*, *101*, 4855–4870, 1996.
- Cremades, H., and V. Bothmer, On the three-dimensional configuration of coronal mass ejections, *Astron. & Astrophys.*, *422*, 307–322, 2004.
- Cremades, H., V. Bothmer, and D. Tripathi, Properties of structured coronal mass ejections in solar cycle 23, *Adv. in Space Res.*, *38*, 461–465, 2006.
- Gopalswamy, N., Y. Hanaoka, and H. S. Hudson, Structure and dynamics of the corona surrounding an eruptive prominence, *Adv. in Space Res.*, *25*, 1851–1854, 2000a.
- Gopalswamy, N., A. Lara, R. P. Lepping, M. L. Kaiser, D. Berdichevsky, and O. C. St. Cyr, Interplanetary acceleration of coronal mass ejections, *Geophys. Res. Lett.*, *27*, 145–148, 2000b.
- Gopalswamy, N., S. Yashiro, M. L. Kaiser, R. A. Howard, and J. L. Bougeret, Radio signatures of coronal mass ejection interaction: Coronal mass ejection cannibalism?, *Astrophys. J.*, *548*, L91–L94, 2001.
- Gopalswamy, N., S. Yashiro, S. Krucker, G. Stenborg, and R. A. Howard, Intensity variation of large solar energetic particle events associated with coronal mass ejections, *J. Geophys. Res.*, *109*, A12,105, 2004.
- Green, L. M., S. A. Matthews, L. van Driel-Gesztelyi, L. K. Harra, and J. L. Culhane, Multi-wavelength observations of an X-class flare without a coronal mass ejection, *Sol. Phys.*, *205*, 325–339, 2002.
- Harrison, R. A., The nature of solar flares associated with coronal mass ejection, *Astron. & Astrophys.*, *304*, 585–594, 1995.
- Harrison, R. A., Soho observations relating to the association between flares and coronal mass ejections, *Adv. Space Res.*, *32*(12), 2425–2437, 2003.
- Harrison, R. A., and M. Lyons, A spectroscopic study of coronal dimming associated with a coronal mass ejection, *Astron. & Astrophys.*, *358*, 1097–1108, 2000.
- Howard, R. A., D. J. Michels, N. R. Sheeley, Jr., and M. J. Koomen, The observation of a coronal transient directed at earth, *Astrophys. J.*, *263*, L101–L104, 1982.
- Hundhausen, A. J., Sizes and locations of coronal mass ejections – SMM observations from 1980 and 1984–1989, *J. Geophys. Res.*, *98*(A8), 13,177, 1993.
- Lara, A., N. Gopalswamy, H. Xie, E. Mendoza-Torres, R. Pèrez-Erriquez, and G. Michalek, Are halo coronal mass ejections special events?, *J. Geophys. Res.*, *111*, A06,107, 2006.
- Lindsay, G. M., J. G. Luhmann, C. T. Russell, and J. T. Gosling, Relationships between coronal mass ejection speeds from coronagraph images and interplanetary characteristics of associated interplanetary coronal mass ejections, *J. Geophys. Res.*, *104*, 12,515, 1999.
- MacQueen, R. M., A. J. Hundhausen, and C. W. Conover, The propagation of coronal mass ejection transients, *J. Geophys. Res.*, *91*, 31–38, 1986.
- Plunkett, S. P., B. J. Thompson, O. C. St. Cyr, and R. A. Howard, Solar source regions of coronal mass ejections and their geomagnetic effects, *J. Atmos. Solar-Terres. Phys.*, *63*, 389–402, 2001.
- Robbrecht, E., S. Patsourakos, and A. Vourlidas, No trace left behind: STEREO observation of a coronal mass ejection without low coronal signatures, *Astrophys. J.*, *701*, 283–291, 2009.
- Schwenn, R., A. Dal Lago, E. Huttunen, and W. D. Gonzalez, The association of coronal mass ejections with their effects near the Earth, *Annales Geophysicae*, *23*(3), 1033–1059, 2005.
- Shen, C., Y. Wang, B. Gui, P. Ye, and S. Wang, Kinematic evolution of a slow CME in near solar space viewed by STEREO-B in October 8, 2007, *Sol. Phys.*, *accepted*, 2010.
- St. Cyr, O. C., and D. F. Webb, Activity associated with coronal mass ejections at solar minimum - SMM observations from 1984–1986, *Sol. Phys.*, *136*, 379–394, 1991.
- St. Cyr, O. C., R. A. Howard, N. R. Sheeley, Jr., S. P. Plunkett, D. J. Michels, S. E. Paswaters, M. J. Koomen, G. M. Simnett, B. J. Thompson, J. B. Gurman, R. Schwenn, D. F. Webb, E. Hildner, and P. L. Lamy, Properties of coronal mass ejections: SOHO LASCO observations from January 1996 to June 1998, *J. Geophys. Res.*, *105*, 18,169, 2000.
- Subramanian, P., and K. P. Dere, Source regions of coronal mass ejections, *Astrophys. J.*, *561*, 372, 2001.
- Vourlidas, A., and R. A. Howard, The proper treatment of coronal mass ejection brightness: A new methodology and implications for observations, *Astrophys. J.*, *642*, 1216–1221, 2006.

- Vourlidas, A., P. Subramanian, K. P. Dere, and R. A. Howard, Large-angle spectrometric coronagraph measurements of the energetics of coronal mass ejections, *Astrophys. J.*, *534*, 456–467, 2000.
- Wang, Y., and J. Zhang, A comparative study between eruptive x-class flares associated with coronal mass ejections and confined x-class flares, *Astrophys. J.*, *665*, 1428, 2007.
- Wang, Y., C. Shen, P. Ye, and S. Wang, Deflection of coronal mass ejection in the interplanetary medium, *Sol. Phys.*, *222*, 329–343, 2004.
- Wang, Y., X. Xue, C. Shen, P. Ye, S. Wang, and J. Zhang, Impact of the major coronal mass ejections on geo-space during September 7 – 13, 2005, *Astrophys. J.*, *646*, 625–633, 2006.
- Wang, Y. M., P. Z. Ye, S. Wang, G. P. Zhou, and J. X. Wang, A statistical study on the geoeffectiveness of earth-directed coronal mass ejections from March 1997 to December 2000, *J. Geophys. Res.*, *107(A11)*, 1340, doi:10.1029/2002JA009244, 2002.
- Webb, D. F., S. W. Kahler, P. S. McIntosh, and J. A. Klimchuck, Large-scale structures and multiple neutral lines associated with coronal mass ejections, *J. Geophys. Res.*, *102(A11)*, 24,161–24,174, 1997.
- Webb, D. F., E. W. Cliver, N. Gopalswamy, H. S. Hudson, and O. C. St. Cyr, The solar origin of the january 1997 coronal mass ejection, magnetic cloud and geomagnetic storm, *Geophys. Res. Lett.*, *25*, 2469–2472, 1998.
- Webb, D. F., E. W. Cliver, N. U. Crooker, O. C. St. Cyr, and B. J. Thompson, Relationship of halo coronal mass ejections, magnetic clouds, and magnetic storms, *J. Geophys. Res.*, *105(A4)*, 7491–7508, 2000.
- Xiong, M., H. Zheng, Y. Wang, and S. Wang, Magnetohydrodynamic simulation of the interaction between interplanetary strong shock and magnetic cloud and its consequent geoeffectiveness: 2. oblique collision, *J. Geophys. Res.*, *111*, A11,102, 2006.
- Xiong, M., H. Zheng, and S. Wang, Magnetohydrodynamic simulation of the interaction between two interplanetary magnetic clouds and its consequent geoeffectiveness: 2. oblique collision, *J. Geophys. Res.*, *114*, A11,101, 2009.
- Yashiro, S., N. Gopalswamy, G. Michalek, O. C. St. Cyr, S. P. Plunkett, N. B. Rich, and R. A. Howard, A catalog of white light coronal mass ejections observed by the soho spacecraft, *J. Geophys. Res.*, *109(A7)*, A07,105, 2004.
- Yashiro, S., N. Gopalswamy, S. Akiyama, G. Michalek, and R. A. Howard, Visibility of coronal mass ejections as a function of flare location and intensity, *J. Geophys. Res.*, *110(A12)*, A12S05, 2005.
- Yermolaev, Y. I., Comment on “geoeffectiveness of halo coronal mass ejections” by n. gopalswamy, s. yashiro, and s. akiyama (j. geophys. res. 2007, 112, doi:10.1029/2006ja012149), *Cosmic Research*, *46*, 540–541, 2008.
- Yermolaev, Y. I., and M. Yermolaev, Statistic study on the geomagnetic storm effectiveness of solar and interplanetary events, *Adv. in Space Res.*, *37*, 1175–1181, 2006.
- Zhang, J., K. P. Dere, R. A. Howard, M. R. Kundu, and S. M. White, On the temporal relationship between coronal mass ejections and flares, *Astrophys. J.*, *559*, 452–462, 2001.
- Zhang, J., K. P. Dere, R. A. Howard, and V. Bothmer, Identification of solar sources of major geomagnetic storms between 1996 and 2000, *Astrophys. J.*, *582*, 520–533, 2003.
- Zhang, J., I. G. Richardson, D. F. Webb, N. Gopalswamy, E. Huttunen, J. C. Kasper, N. V. Nitta, W. Poomvises, B. J. Thompson, C.-C. Wu, S. Yashiro, and A. N. Zhukov, Solar and interplanetary sources of major geomagnetic storms ($Dst \leq -100$ nT) during 1996–2005, *J. Geophys. Res.*, *112*, A10,102, 2007.
- Zhao, X. P., and D. F. Webb, Source regions and storm effectiveness of frontside full halo coronal mass ejections, *J. Geophys. Res.*, *108(A6)*, 1234, 2003.
- Zhou, G., J. Wang, and Z. Cao, Correlation between halo coronal mass ejections and solar surface activity, *Astron. & Astrophys.*, *397*, 1057, 2003.